Three dimensional internal and near-wall flow features of a structured porous coated cylinder

Arcondoulis, Elias J. G.; Liu, Yu; Yang, Yannian; Ragni, D.; Rubio Carpio, A.; Avallone, F.

DOI
10.2514/6.2022-3038

Publication date
2022

Document Version
Final published version

Published in
28th AIAA/CEAS Aeroacoustics 2022 Conference

Citation (APA)
Arcondoulis, E. J. G., Liu, Y., Yang, Y., Ragni, D., Rubio Carpio, A., & Avallone, F. (2022). Three dimensional internal and near-wall flow features of a structured porous coated cylinder. In *28th AIAA/CEAS Aeroacoustics 2022 Conference* Article AIAA 2022-3038 (28th AIAA/CEAS Aeroacoustics Conference, 2022). https://doi.org/10.2514/6.2022-3038

Aeroacoustics Conferences
June 14-17, 2022, Southampton, UK
28th AIAA/CEAS Aeroacoustics 2022 Conference

10.2514/6.2022-3038

Three dimensional internal and near-wall flow features of a structured porous coated cylinder

Elias J. G. Arcondoulis*, Yu Liu† and Yannian Yang‡
Southern University of Science and Technology, Shenzhen, Guangdong Province, 518055, P. R. China

Daniele Ragni§, Alejandro Rubio Carpio¶ and Francesco Avallone‖
Delft University of Technology, Delft 2629HS, The Netherlands

The application of a porous coating to a cylinder can significantly reduce the vortex shedding tone when placed in a uniform flow. The mechanism of how this porous media attenuates vortex shedding has been studied more in recent years yet it is still not fully understood. Typical porous materials within a certain range of porosity and airflow resistivity, such as metal foam and porous polyurethane, have been studied extensively; however, the fundamental flow mechanisms responsible for vortex shedding attenuation are very difficult to determine. For example, it is nearly impossible to visualize the internal flow field of porous media with a randomized open-cell internal structure. A Structured Porous Coated Cylinder (SPCC) was designed in recent years to alleviate this internal flow field problem, as the SPCC has clear line of sight along the span and radial direction. SPCC variations have been previously studied and shown to reduce the vortex shedding tone of a bare cylinder in a very similar manner as a randomized porous coated cylinder. In this paper, we present a Tomographic Particle Image Velocimetry study of an SPCC tested in a water tunnel, revealing the previously unseen internal and near-wall flow fields of an SPCC. The flow is visualized in the porous layers, revealing complex interaction between the freestream flow field and the porous structure. Using cross-correlation methods within the flow field, we reveal the entrainment of the flow within the porous layers. Furthermore, implementation of Proper Orthogonal Decomposition shows that vortex shedding occurs within the porous layers.

I. Introduction

The application of passive flow control techniques for cylindrical bodies [1] is applicable for sections of high speed train pantographs [2, 3], aircraft landing gear [4, 5] and electrical power lines. Various studies of a Porous Coated Cylinder (PCC) have been shown to decrease the magnitude of tonal noise and its frequency [6–8]. An interesting observation is that Sueki et al. [2] experimentally showed that the material type had little or no impact on the measured noise reduction for randomized porous structures, if they had similar porosity and Pores Per Inch (PPI). This important study revealed that the porous material thickness, porosity and spacings of the pores were of greatest importance in tonal and broadband noise reduction.

The internal flow within the randomized porous medium would be extremely difficult to measure experimentally without modifying the porous structure and it is therefore likely that these difficulties have led to few publications in this area, other than numerical studies [9–13]. Naito and Fukagata [14] via simulation presented boundary layer profiles of PCCs using a Darcy-Forcheimer porous medium approximation. They also proposed that the energy of the entrained fluid within the porous layer is dissipated and the ejected low-energy fluid from the PCC leeward side raises the back pressure. At low-Reynolds numbers, Xu et al. [15] conducted a 3-D numerical investigation of flow through a single open cell metal foam pore. This revealed the internal flow field within a single pore yet it is difficult to relate this result to a cylindrical geometry as compared to a single, isolated pore.

Arcondoulis et al. [8] designed a Structured Porous Coated Cylinder (SPCC), such that a clear line of sight is possible along the cylinder span and also from the outer porous coated cylinder surface into the internal solid cylinder. They

---

*Research Assistant Professor, Department of Mechanics and Aerospace Engineering, AIAA Senior Member
†Associate Professor, Department of Mechanics and Aerospace Engineering, AIAA Senior Member
‡Research Assistant Professor, Department of Mechanics and Aerospace Engineering, AIAA Member
§Associate Professor, Department of Aerodynamics, Wind Energy, Flight Performance & Propulsion, AIAA Member
¶PhD Candidate, Department of Aerodynamics, Wind Energy, Flight Performance & Propulsion, Student AIAA Member
‖Assistant Professor, Department of Aerodynamics, Wind Energy, Flight Performance & Propulsion, AIAA Member

showed that the tone suppression and frequency shift were very similar to porous coated cylinders usinng randomized porous media with similar porosity and PPI. Via wind tunnel experiments, they showed that the tonal noise reduction of an SPCC is independent on the spanwise and circumferential variations in porosity, provided that the average porosity of the porous layer was the same between different cylinders [16, 17]. Some of those authors then conducted some 3-D tomographic Particle Image Velocimetry (PIV) at three locations within the porous layer and at the near-wall [18], that revealed boundary layer development within the porous layer and the entrainment of fluid at the cylinder leeward side, consistent with Naito et al. [14]. Recently, a modification to the SPCC has been used for active flow control [19].

This paper is a continuation of the work of Arcondoulis et al. [18], now revealing previously unseen 3-D flow structures within the porous layer and at the near-wall regions. The effect of pore geometry on how the flow stagnates on the windward side is investigated, and the complex flow field around the porous structure is presented in 3-D, using a new method of streamline development, such that starting points are the SPCC porous surfaces. The Q-criterion [20] is plotted for various values and colored via time-averaged vorticity that reveals the shear-layer roll up and development of vortical structures at the windward side and within the porous layer. A Proper Orthogonal Decomposition (POD) analysis is conducted both within and outside the porous layer revealing vortex shedding spectral content within a single pore.

II. Methodology

A. Cylinder Design

The porosity of the SPCC is 87%, which identical to previous studies [8, 16]. A CAD representation of the SPCC is presented in Fig. 1. This geometry was 3-D printed in one-piece using a transparent ultraviolet curing epoxy resin. By modifying the C-shaped chip parameters in Fig. 1, SPCCs can be designed with a wide range of PPI and porosity.

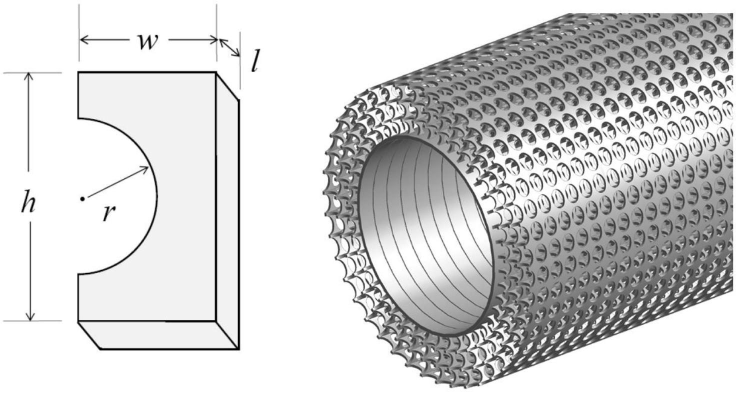

Fig. 1 CAD representation of the SPCC used for tomographic PIV experiments.

The SPCC outer diameter was D = 96 mm with an inner bare diameter of d = 64 mm, and thus the ratio of the porous coating thickness to the bare cylinder diameter, t/d, is 0.25. This t/d ratio is consistent with the aeroacoustic investigation presented in Arcondoulis et al. [8, 16] and within the typical t/d range of others [2, 3, 6, 7, 14, 21–23]. The SPCC has a span of 385 mm.

B. Tomographic PIV set-up

Tomographic PIV experiments were conducted in a water tunnel in the Department of Civil Engineering and Geosciences at TU Delft, The Netherlands. This experimental method is identical to previous investigations [18, 24] and further details can be sought in [18]. The freestream velocity was U_0 = 0.8 m/s corresponding to a Reynolds number based on the outer diameter of Re = 7.3 × 10^4 (at a water temperature of 18°C) which is comparable with other porous coated cylinder studies [3, 6, 7, 14, 25] and bare cylinders [26–29].

Four-camera tomographic PIV was used to record both the internal and near-wall flow field of a transparent 3-D printed SPCC in a low-speed water tunnel, within a working section of 400 mm wide and an open channel height of 500 mm. Fine silt particles of approximately 100 μm in size were used to seed the water tunnel and a Quantel EverGreen200

Double-Pulse Nd:YAG laser (532 nm wavelength, 200 mJ per pulse) was used for illumination. One spherical and two-to-three cylindrical lenses were aligned to produce a 20 mm thick laser sheet. LaVision Imagers LX 16M (16MPx, 7.4 μm pixel pitch) were placed with Nikon Micro-Nikkor prime lenses (105 mm). Scheimpflug adapters were used to align the focal plane with the laser sheet (i.e., perpendicular to the water tunnel glass walls) and synchronization between the laser pulses and image acquisition was achieved using a LaVision Programmable Timing Unit in combination with the LaVision DaVis 8.4 software package. Table 1 summarizes the parameters used during the PIV experiments in this study. Flow field data was processed using an in-house MATLAB code.

Table 1 Summary of PIV parameters.

Parameter	Tomo PIV Set-up
Frame type	Double-Frame
Lens focal length	105 mm
Focal ratio ($f/\#$)	16
Field of view (FOV)	various
Acquisition frequency (f_{aq})	15 Hz
Pulse separation (Δt)	600 μs
Number of samples (N)	1000
No. images for time-averaging (N_s)	500

In this paper we present results for two FOVs, namely FOV #1 and #2, as depicted in Fig. 2. The position of FOV #1 was chosen to determine the interaction between the freestream flow and the first contact with the porous layer, how the porous layers affect the stagnation point of the flow, and how the flow attaches to the SPCC outer diameter. The position of FOV #2 was chosen to reveal the growth and development of the internal and near-wall boundary layer and shear layer. The dimensions of each FOV vary slightly in the x- and y-directions, due to some FOV cropping during post-processing, where in some cases velocity data on the edges of the FOV were unusable. Note that due to the thickness of the laser sheet, each FOV is 20 mm thick (z/D = 0.21).

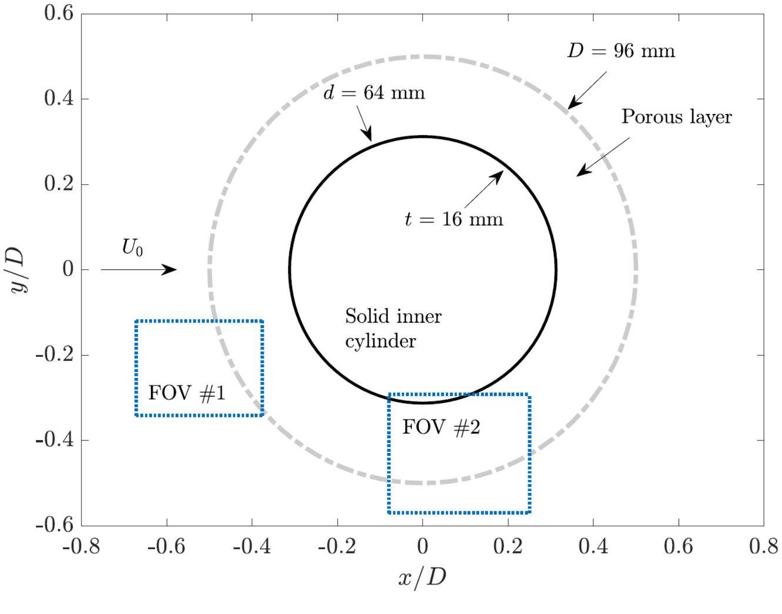

Fig. 2 Position of tomographic PIV FOVs #1 and #2. Image is to scale.

C. Post-processing techniques

1. Internal streamlines

The flow field within and near the porous layer is complex and varies significantly with local geometric features and time, and a novel approach is therefore used to visualize the streamlines inside the porous layer. An in-house MATLAB code was developed that imports a CAD model of the SPCC in an .STL file format (commonly used for 3-D printing). The coordinates of the model are extracted and then plotted with the FOVs from the experiments to overlay the geometry and flow field in 3-D. To visualize the complex flow pattern in the internal porous layer, the coordinates of the CAD model are matched to the nearest point in the 3-D flow field volume via linear interpolation. These points in the flow field, that are typically extremely close to the CAD model coordinates, are used as the starting points for streamlines. This helps reveals the internal flow field that is developed from the SPCC surface, as compared to arbitrary points within the porous layer, or in the near-wall flow field.

2. Q-criterion & vorticity

The velocity field is defined as $U(x,y,z,t)$ (m/s), where the x-, y- and z-components of velocity are $u(x,y,z,t)$, $v(x,y,z,t)$ and $w(x,y,z,t)$, respectively. The Q-criterion [20] was calculated to investigate the development of vortical structures at the near-wall and within the porous layer and is calculated as

$$Q = \frac{1}{2}\left[\left(\frac{\partial u}{\partial x}\right)^2 + \left(\frac{\partial v}{\partial y}\right)^2 + \left(\frac{\partial w}{\partial z}\right)^2\right] - \frac{\partial u}{\partial y}\frac{\partial v}{\partial x} - \frac{\partial w}{\partial y}\frac{\partial v}{\partial z} - \frac{\partial w}{\partial x}\frac{\partial u}{\partial z}, \tag{1}$$

Isosurfaces of single-valued Q-criterion are plotted that are colored by time-averaged vorticity (1/s), calculated as

$$\overline{\omega}_z = \frac{\partial \overline{v}}{\partial x} - \frac{\partial \overline{u}}{\partial y} \tag{2}$$

where the overline represents temporal averaging. In this study vorticity is normalized via $|\overline{\omega_z}|D/U_0$.

3. Cross-correlation

The relationship between the internal and external flow field of the SPCC is not well understood. Since tomographic PIV data is obtained with sufficient temporal resolution, a cross-correlation analysis between any two points within a single FOV can be conducted. By selecting a point inside and another point outside the SPCC porous layers, insight into whether the internal and external flow fields are correlated can be obtained. The cross-correlation term, $R_{ij}(\tau)$, is defined as

$$R_{ij}(\tau) = \frac{\frac{1}{N}\sum_{n=1}^{N}\left(U(i,t_n)U(j,t_n+\tau)\right)}{\sqrt{\langle U^2(i,t)\rangle\,\langle U^2(j,t)\rangle}} \tag{3}$$

where i and j are location coordinates, n is a temporal index of time, t, from 1 to N and τ is the time-lag at which peak cross-correlation is observed. In this study, between each location i and j, τ is selected to obtain $R_{ij}|_{\max}$.

4. POD analysis

A preliminary POD analysis was conducted within FOV #2 to determine the influence of the internal flow field on the vortex shedding tone of the SPCC. POD has been previously used to analyze the wake flows of various porous coated cylinder configurations [19, 23, 30] and airfoil wakes [31]. In this study, POD was conducted on the x-component of velocity, $\mathbf{u} = u(x,y,t)$ using all $N_s = 500$-images over a 66.6 s period. Firstly, the time-averaged velocity is subtracted from each velocity signal to obtain the fluctuating velocity, $\mathbf{u}'$, via

$$\mathbf{u}' = \mathbf{u} - \overline{\mathbf{u}} \tag{4}$$

A correlation matrix, $\mathbf{C}$, is calculated via

$$\mathbf{C} = \frac{1}{N_s - 1}\left(\mathbf{u}'\mathbf{u}'^T\right) \tag{5}$$

then $\mathbf{C}$ is used to solve the following eigenvector calculation via

$$\mathbf{CA} = \mathbf{\Lambda A} \tag{6}$$

where $\mathbf{\Lambda} = \lambda_1 \ldots \lambda_n$ are the eigenvalues and $\mathbf{A} = a_{11} \ldots a_{mn}$ are the eigenvectors of the correlation matrix (corresponding to the temporal mode coefficients). Note that in this study we do not reconstruct the flow field for various modes and we are only concerned in eigenvalues, eigenvector magnitudes and their variation in magnitude within FOV #2: see Section IIIB4.

III. Results

A. FOV #1

1. Velocity & Streamlines

To provide an overview of the velocity field in FOV #1, 3-D streamlines of $\overline{U}/U_0$ are presented in Fig. 3. Figure 3(a) is a spanwise view showing the flow accelerating past the SPCC outer diameter and some of the chaotic flow behavior within the porous layer (further visualization of the flow within some of the porous layer is shown in Fig. 4). The acceleration around the cylinder is qualitatively very similar to that of a bare cylinder. The flow stagnation at the outer diameter and within the porous layer is much more complex, however, and is further investigated in Fig. 5. By observation Figs. 3(b) and 3(c), variation of the velocity field in the z-direction is seen, as the streamlines appear to bunch toward a small region with increasing x/D. This is an indication of some spanwise variation in the flow field that is likely to have an impact on the spanwise coherence of the SPCC.

The streamlines presented in Fig. 4 are never-seen-before experimentally-obtained internal flow fields within a porous coated cylinder, obtained using the method outlined in Section IIC1. There are regions of highly localized

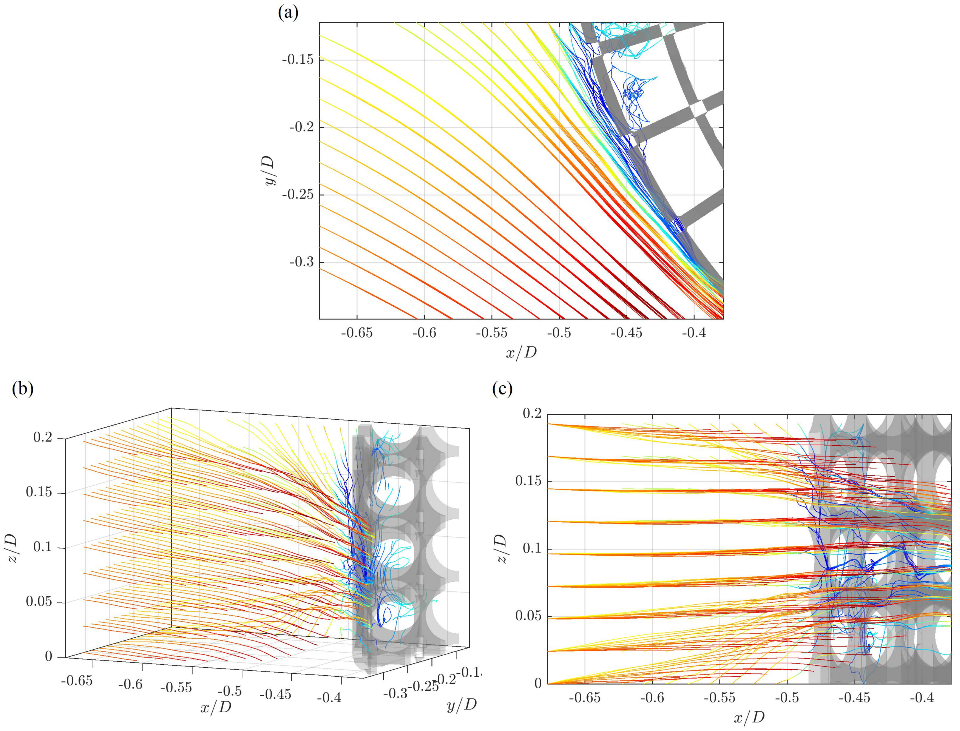

Fig. 3 Streamlines of $\overline{U}/U_0$ within FOV #1 (a) spanwise (z-direction) view, (b) arbitrary 3-D view and (c) radial (y-direction) view. The color scheme of blue to red corresponds to zero to maximum velocity within FOV #1. Flow is in the positive x-direction. Images are adapted and furthered from Ref. [18].

vortical structures (that are also presented in Fig. 6) and chaotic flow patterns in the pore regions near the structural members, where flow is seen to wrap around the structural members. In Fig. 4(a) some streamlines are seen to follow the outer diameter of the SPCC, along a ridge of sold material (e.g., along $z/D \approx 0.25$). In the absence of a ridge, the flow wraps around the ring of the pore into the porous layer, therefore creating regions of localized vorticity (further presented in Fig. 6).

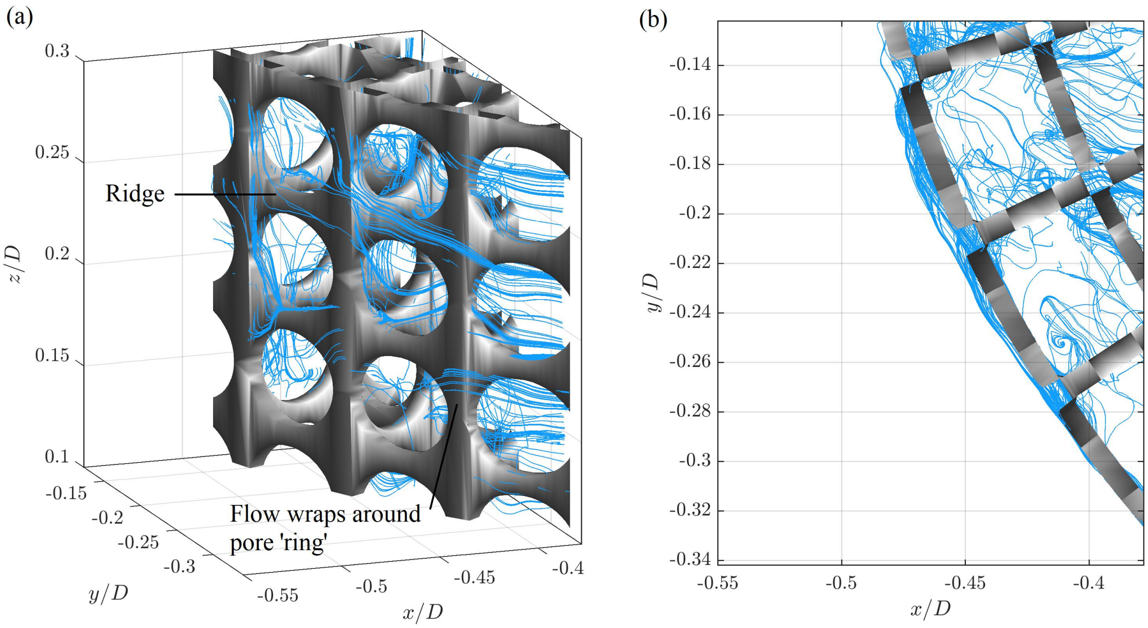

Fig. 4 Streamlines representing part of the SPCC windward side internal flow field recorded in FOV #1 (a) arbitrary 3-D view and (b) spanwise (z-direction) view, plotted using the method outlined in Section IIC1. Flow is in the positive x-direction.

To quantitatively investigate how the freestream flow penetrates the porous layer, flow data were recorded on lines in the spanwise direction, with $y/D = -0.16$. For convenience, the x-coordinate here is replaced with an r/t-coordinate, where r is a radial distance that represents the distance from the SPCC inner diameter, and t is the thickness of the porous layer. The value $r/t = 0$ denotes the inner cylinder outer surface ($x/D = -0.3125$) and $r/t = 1$ represents the outer diameter surface ($x/D = -0.5$). Figure 5 presents time-averaged non-dimensionalized flow velocity components in the x- and y-directions, $\overline{u}/U_0$ and $\overline{v}/U_0$, respectively, and their variation in the z-direction as the flow approaches the outer windward surface of the SPCC and within the porous layer. This figure clearly shows the gradual flow deceleration towards the outer porous layer and the rapid deceleration once the flow enters the porous layer where the grey shaded areas represent the structural member of the pore, and the unshaded areas represent the pores.

The radial vector follows an open-pore path, so that along the z/D-axis, we can observe local minima and maxima corresponding to the flow interacting with a structural member or flowing into the porous layer, respectively. At r/t = 1.24, $\overline{u}/U_0$ shows little variation in z/D, as the flow approaching the windward surface of the SPCC has not interacted with the porous surface. However, at r/t = 1.06, significant variation in $\overline{u}/U_0$ with respect to z/D is observed, and this variation is seen to increase with decreasing r/t. In other words, the streamwise velocity component is seen to interact with the porous structure; at the structural member, it stagnates, and at the open pores, it flows into the porous layer. Further inside the porous layer, at r/t = 0.82, the flow has nearly stagnated at all z/D-locations. The stagnation of the streamwise velocity occurs rapidly between r/t = 0.82 and 0.89. At values of $r/t < 0.82$ the streamwise velocity is totally stagnated. This provides evidence for flow entrainment at the windward side of the SPCC within the porous layer (further discussed in Section IIIA3). Similar behavior is noticed for the y-component of velocity, $\overline{v}/U_0$, where stagnation occurs between r/t = 0.82 and 0.89 and the first noticeable local influence of the porous structure on the oncoming flow field takes place r/t = 1.06.

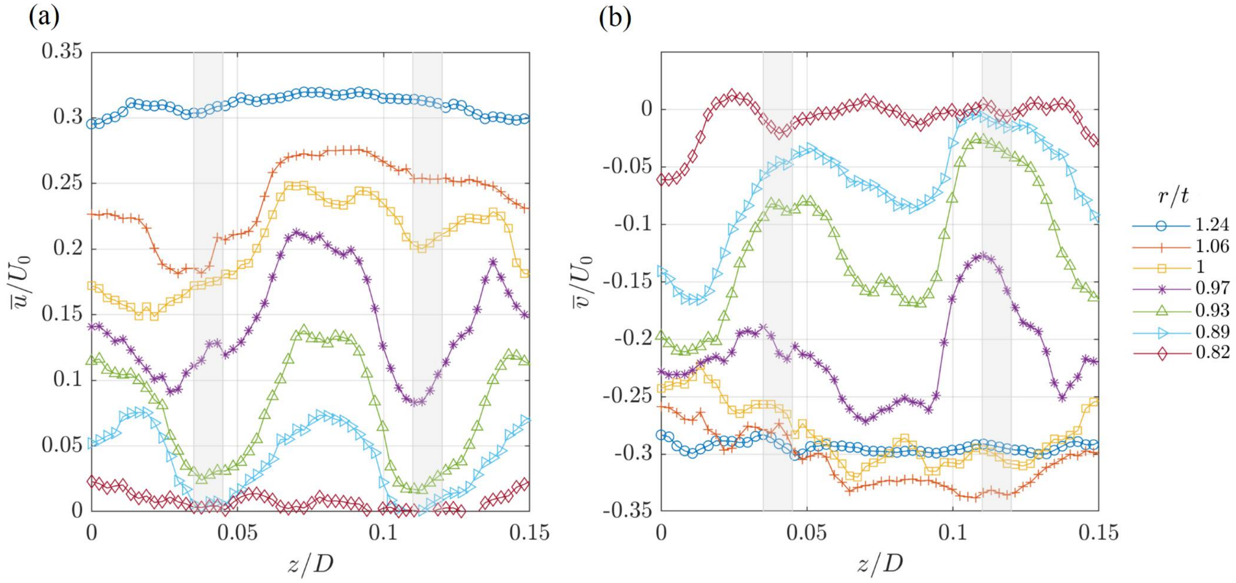

Fig. 5 Variation of the flow field along z/D (spanwise direction), approaching and entering the windward side of the SPCC between $z/D = 0$ to 0.15 (a) $\overline{u}/U_0$ and (b) $\overline{v}/U_0$. Each line is represented by an r/t-coordinate and the shaded areas represent the pore structural members.

2. Q-criterion & vorticity

The time-averaged vorticity is visualized in Fig. 6. On the left-side, the Q = 0.01 isosurfaces are seen to increase in density further along the circumferential direction of the SPCC, as the flow develops shear around the cylinder outer surface. As the flow component toward the cylinder becomes more tangential in nature (as compared to normal direction) due to the circular geometry, this leads to an increase in vortical structures further along the cylinder circumference within FOV #1. On the right-side, the time-averaged vorticity is plotted at several xy-planes with the corresponding SPCC slice at that plane. It can be seen that there are regions of strong vorticity near the porous structural members, as the flow attempts to both enter the porous region and also passes by the outer diameter resulting in strong shear. The flow needs to rotate about a pore ridge in order to enter the porous layer (shown in Fig. 4) that corresponds to small localized regions of high vorticity. A curved line of vorticity can be seen in each of the xy-slices that correspond to this flow mechanism.

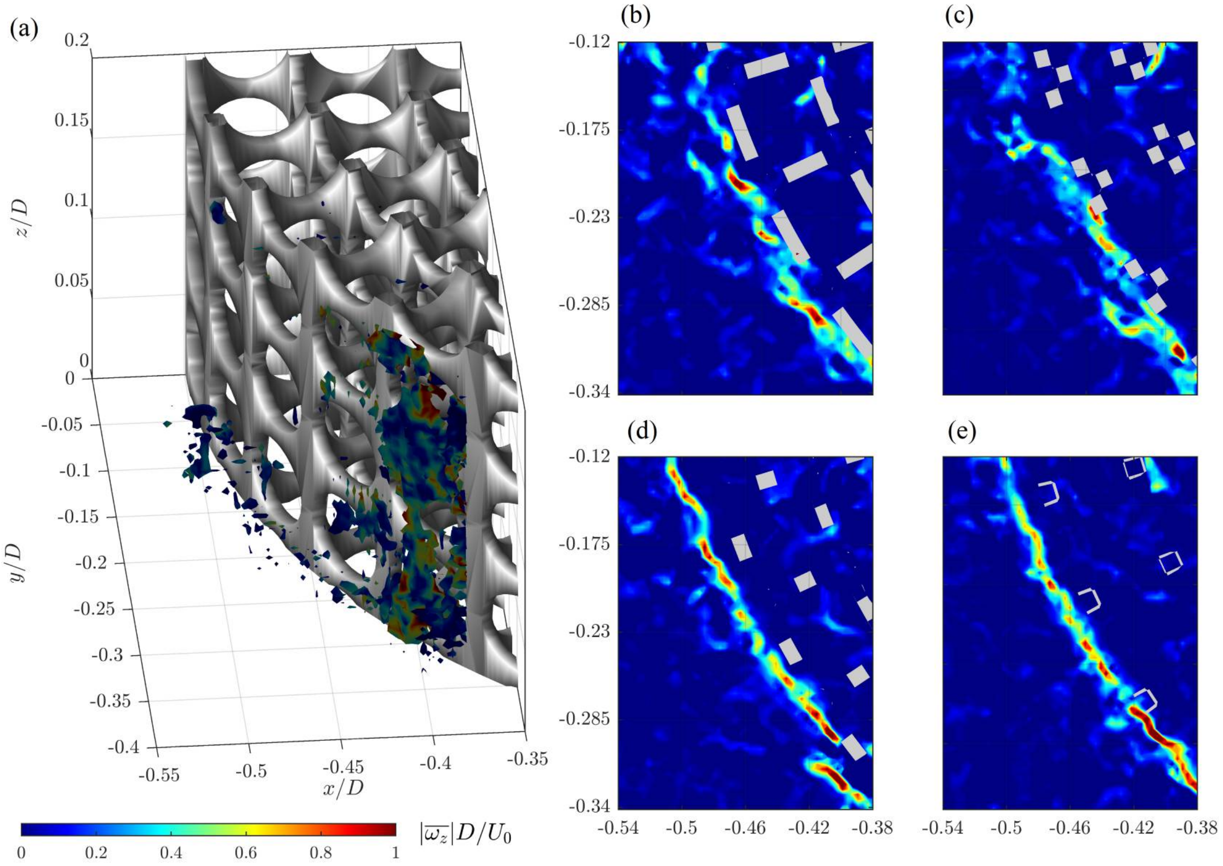

Fig. 6 (a) Q-criterion, $Q = 0.01$, colored by $|\overline{\omega_z}|D/U_0$ in FOV #1. The subplots on the right are xy-planes of $|\overline{\omega_z}|D/U_0$ and the corresponding SPCC section slice, obtained at (b) z/D = 0, (c) z/D = 0.04, (d) z/D = 0.1 and (e) z/D = 0.16. Flow is in the positive x-direction.

3. Cross-correlation

The cross-correlation of the flow field within FOV #1 was calculated via Eq. (3). Three reference points were selected to help understand the influence of the external flow field on the fluid region within the porous layer, as presented in Fig. 7. Reference point i_1 is located in the top-left corner of FOV #1 (external flow field), i_2 is placed along $r/t = 1$ within an open pore region and i_3 is located also in an open pore region further into the porous layers (top-right of FOV #1). In Fig. 7(a) isosurfaces of $R_{ij} \geq 0.9$ for reference locations i_1, i_2 and i_3 are shown. Clearly, using reference location i_1 it is seen that the external flow field correlation region does not extend into the porous layer. This suggests that the temporal behavior of the external flow field is uncorrelated with the internal and near-wall flow fields, and that the fluid within the porous layer is entrained [14]. Using reference locations i_2 and i_3 it is revealed that the flow along the SPCC outer diameter is strongly correlated, which is supported by the observation of streamlines along the porous outer diameter ridges (in Fig. 4). Furthermore, some strong correlation is also observed between the flow field at $r/t = 1$ and the near-wall region centered about $x/D = -0.5$ and $y/D = -0.25$ showing that the interaction of the shear flow as it passes the SPCC outer diameter is strongly correlated with the local vortical regions in the outermost porous layer. Using i_3 as a reference location also reveals that there is a strong correlation between the inner-region and outer-regions of the external flow fields, which is an interesting result. The complex streamline patterns of the internal flow field shown in Fig. 4 appear to be highly chaotic yet there is indeed a relationship between the flow fields of each porous layer. This complex interaction between the near-wall and internal flow field is certainly far from well understood; it is future work to investigate temporal-spatial relationships along the spanwise direction in FOV #1 to further understand the underlying flow field behavior.

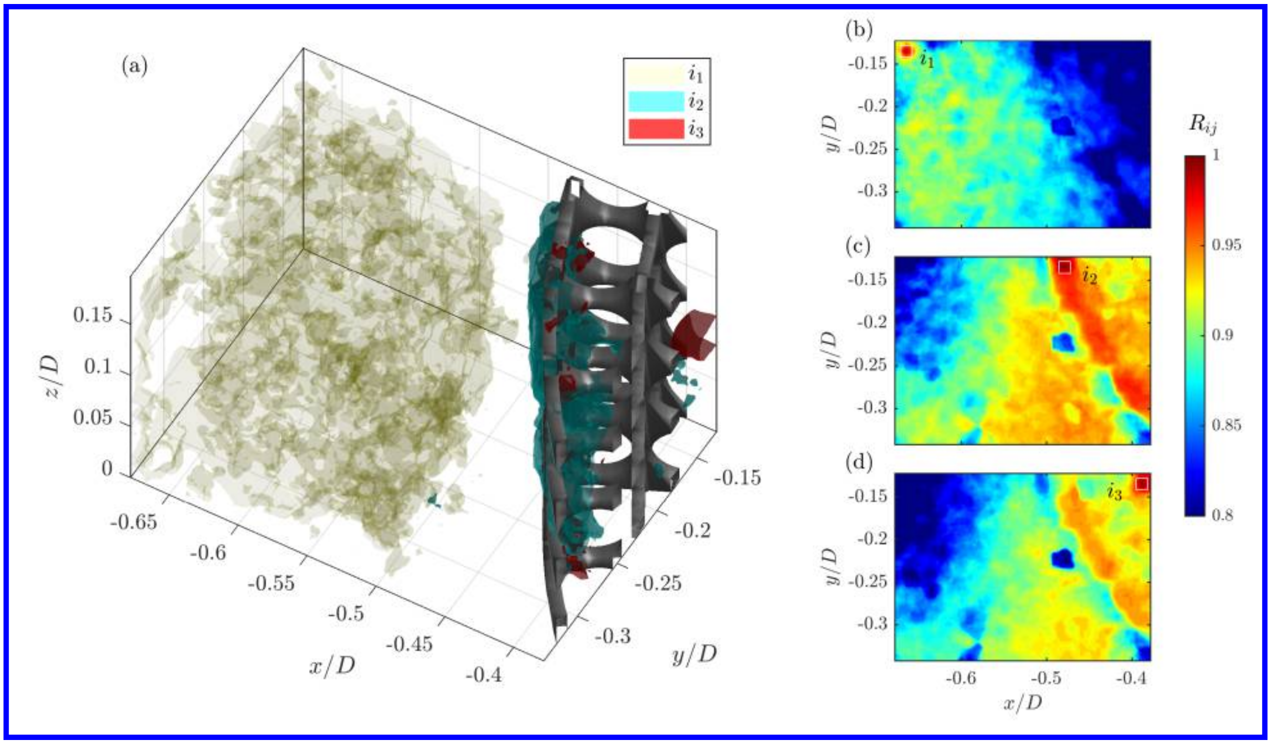

Fig. 7 Cross-correlation, R_{ij}, of $U(x, y, z, t)$ in FOV #1. Locations, i denote a fixed reference location in the xy-plane $(z/D = 0.08)$. (a) Iso-surfaces of $R_{ij} \geq 0.9$ for three reference locations, i_1, i_2 and i_3, and values of R_{ij} recorded in the xy-plane $(z/D = 0.08)$ of (b) i_1, (c) i_2 and (d) i_3. Flow is in the positive x-direction.

B. FOV #2

1. Streamlines

The external flow field, and to some degree the internal flow field, within FOV #2 are visualized using 3-D streamlines $\overline{U}/U_0$, as presented in Fig. 8. These images reveal that there is much less interaction between the porous structure and the internal and near-wall flow field as compared with FOV #1. A boundary layer develops predominately from the SPCC inner diameter, rather than the outer diameter (as previously observed and discussed by Arcondoulis et al. [18]). Variation in the spanwise flow field in FOV #2 is less pronounced than in FOV #1, where it appears that the flow field is dominated by the streamwise flow component. Further investigation into the internal flow field is presented in Fig. 9.

By using the method outlined in Section IIC1 we can visualize more clearly the internal flow field of the mid-circumferential porous layer region. As the flow exits the porous layer, we do not observe the streamlines wrapping around the porous ring or any streamlines along the porous ridges. The flow passes through the pores with little interference. Near the SPCC inner diameter at $x/D = -0.35$ we observe some streamlines originating from the porous structural members. As observed from their streamline pathway, the flow initially travels in the x-direction only, and then as the flow propagates downstream, it interacts with the accelerated flow region (denoted in red in Fig. 8) and gains radial velocity.

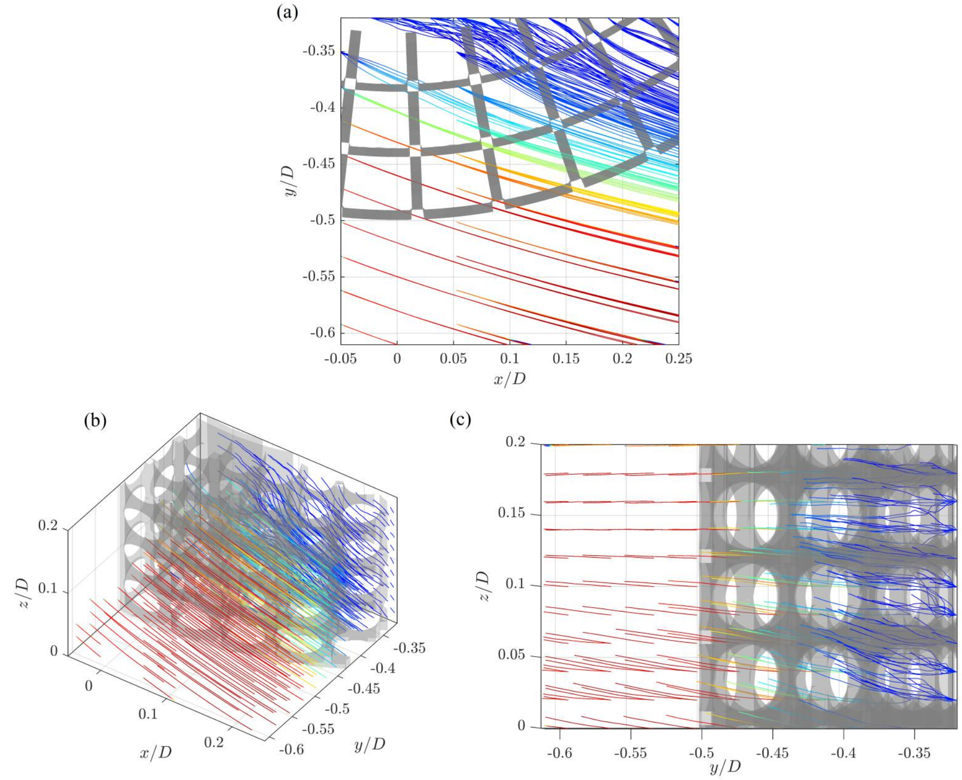

Fig. 8 Streamlines of $\overline{U}/U_0$ within FOV #2 (a) spanwise (z-direction) view, (b) arbitrary 3-D view and (c) radial (x-direction) view. The color scheme of blue to red corresponds to zero to maximum velocity within FOV #2. Flow is in the positive x-direction.

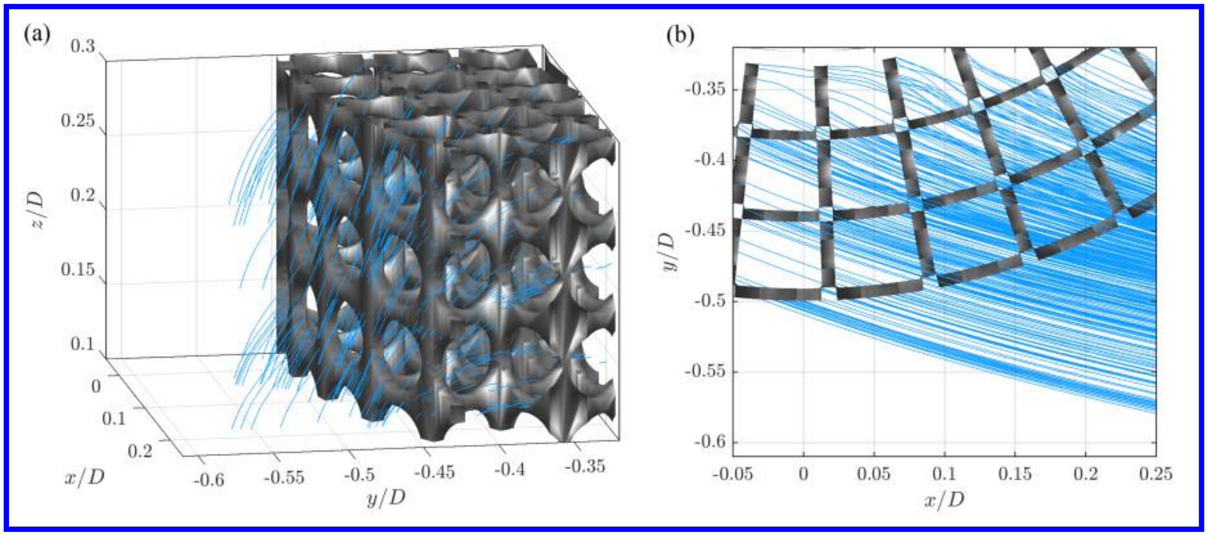

Fig. 9 Streamlines representing part of the SPCC mid-circumferential region internal flow field recorded in FOV #2 (a) arbitrary 3-D view and (b) spanwise (z-direction) view, plotted using the method outlined in Section IIC1. Flow is in the positive x-direction.

2. *Q-criterion & vorticity*

The Q-criterion ranging from 0.001 to 0.02 is plotted and colored by $|\overline{\omega_z}|D/U_0$ in FOV #2, as presented in Fig.10. A range of Q-value isosurfaces were plotted to help visualize the distribution of vorticity from the inner to outer SPCC diameters. The region of $Q = 0.02$ corresponds to region furthest from the inner diameter, that corresponds to the regions of maximum vorticity. The xy-slices of vorticity on the right-side reveal a strong shear layer with high vorticity, for all xy-planes presented, that corresponds to the region of greatest change in tangential velocity per internal boundary layer within the porous layer [18]. The strongest region of vorticity occurs at most-upstream region of FOV #2, where the kinetic energy of the shear layer is greatest, prior to its energy being distributed within the porous layer and several complex interactions with porous members. At $z/D = 0.1$ a small region of vorticity emanating from the inner diameter can be seen at $x/D = 0.06$ and $y/D = -0.36$. This location corresponds to the commencement of the streamlines from the pore structural members shown in Fig. 9(b). It is future work to understand how this localized flow field influences the development of the shear layer within the porous region.

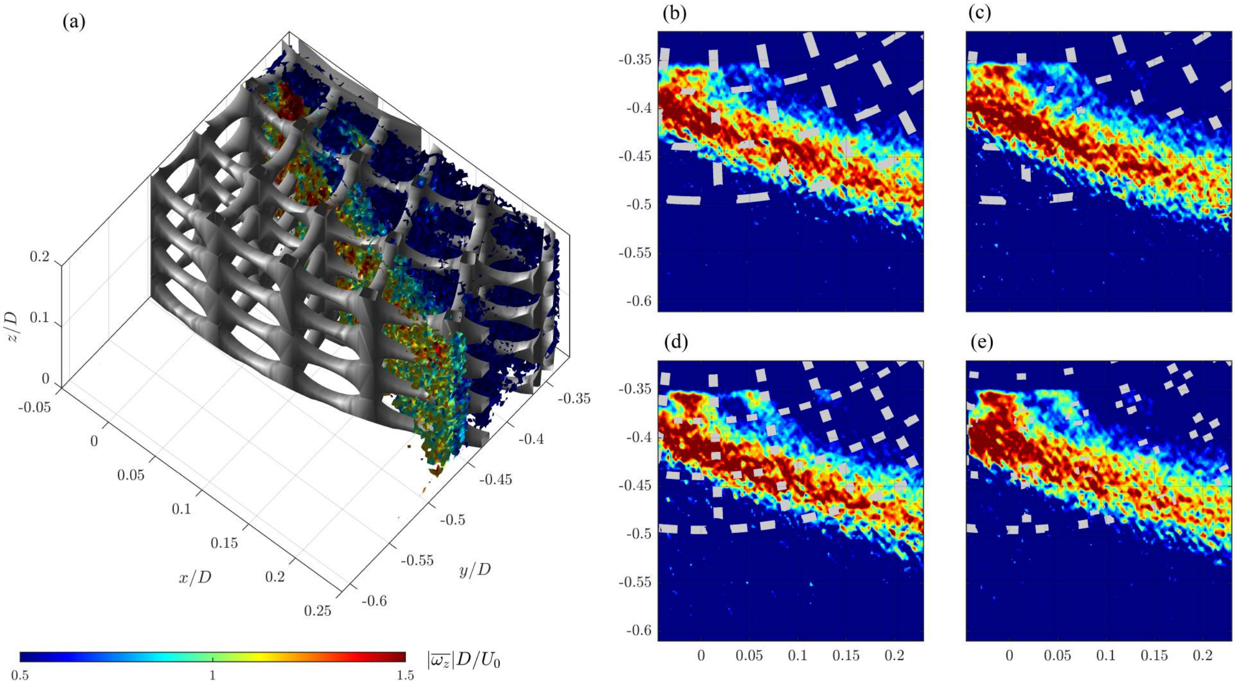

Fig. 10 (a) Q-criterion from 0.001 to 0.02, colored by $|\overline{\omega_z}|D/U_0$ in FOV #2. The subplots on the right are xy-planes of $|\overline{\omega_z}|D/U_0$ and the corresponding SPCC section slice, obtained at (b) $z/D = 0$, (c) $z/D = 0.04$, (d) $z/D = 0.1$ and (e) $z/D = 0.12$. Flow is in the positive x-direction.

3. *Cross-correlation*

The cross-correlation of the flow field within FOV #2 is presented in Fig. 11. The overall shape of the isosurfaces in Fig. 11(a) resemble the shear layer (strong region vorticity) region in Fig. 10. Due to weaker $R_{ij}|_{\max}$-values in FOV #2 as compared to FOV #1, several different R_{ij}-values are selected in Fig. 11(a) to help illustrate key correlation features. By considering i_1 the flow near the inner diameter shows weak correlation with the flow in the shear layer. By placing a reference point at i_2 we can observe a thin layer (in red) that weaves through the porous layers downstream. This region is uncorrelated to the inner diameter near-wall region, implying that the flow near the inner diameter is part of a boundary layer developed by the inner diameter. Cross-correlation results using reference point i_3 reveal a strong relationship with the external flow field and the flow in the outermost porous layers. From this we can ascertain that the outermost porous layers at the mid-circumferential region ($x/D \approx 0$) have little impact on the shear layer expansion, that may be responsible for the enlarged shear layer that is observed for porous coated cylinders (with outer diameter D), relative to bare cylinders (with diameter d) [9, 11, 14, 16, 23].

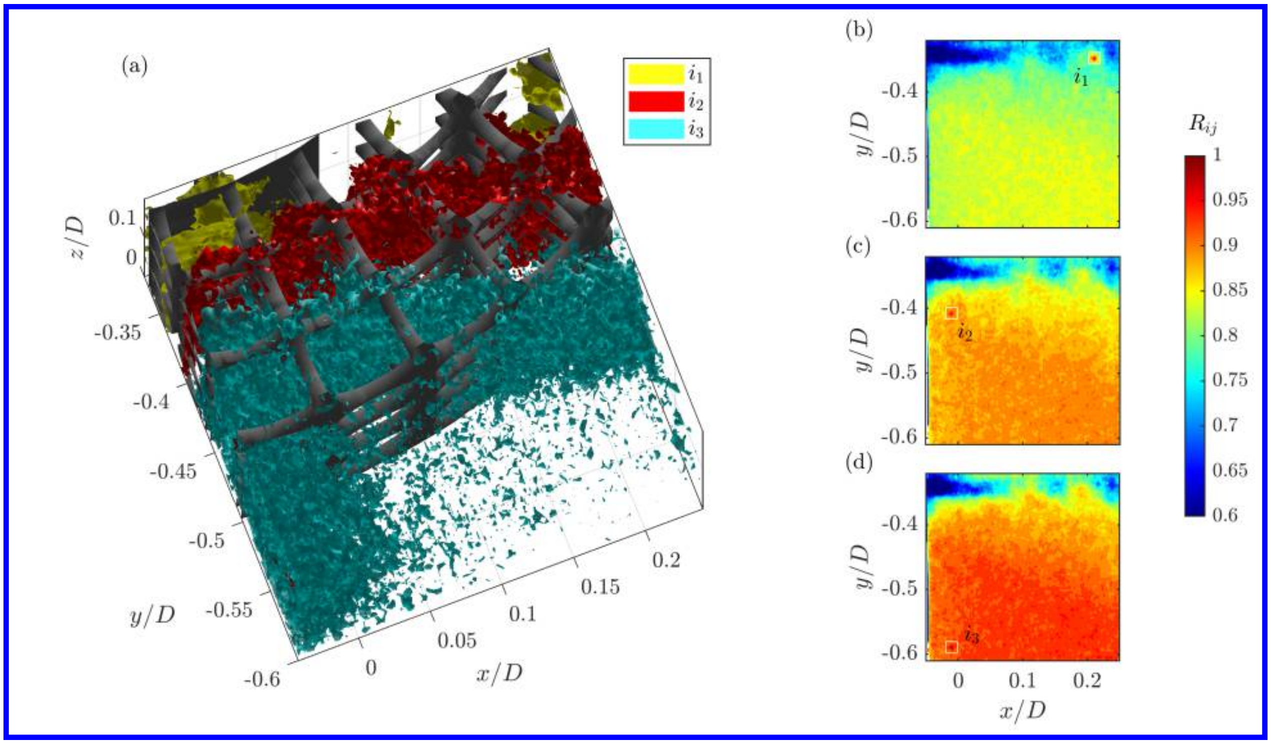

Fig. 11 Cross-correlation, R_{ij}, of $U(x, y, z, t)$ in FOV #2. Locations, i denote a fixed reference location in the xy-plane ($z/D = 0.08$). (a) Iso-surfaces of $R_{ij} = 0.6$ for i_1, $R_{ij} = 0.8$ for i_2 and $R_{ij} \geq 0.9$ for i_3 and values of R_{ij} recorded in the xy-plane ($z/D = 0.08$) of (b) i_1, (c) i_2 and (d) i_3. Flow is in the positive x-direction.

4. POD analysis

POD was conducted on the streamwise velocity component in FOV #2. For the purposes of conducting a POD analysis, FOV #2 was divided into four small regions labeled I, II, II and IV, as identified in Fig. 12(a). In addition, POD was also conducted on the entire area of FOV #2. These regions were specifically selected to determine the effect of the inner solid diameter and the outer porous diameter on the development of vortex shedding.

SPCCs have been previously shown to exhibit two vortex shedding tones [16] suggested to be linked to independent vortex shedding phenomena from the SPCC inner and outer diameter. Eigenvalues, $\lambda_n / \sum \lambda_n \times 100$ (%), were calculated on $u'(x, y, t)$ within regions I, II, III, IV and FOV #2, as presented in Fig. 12(b). Due to the complexity of calculations within a 3-D volume, it is convenient to first calculate the eigenvalues averaged over the z-direction, z_{av}. Regions I and II show by far the strongest percentage of energy within $n < 10$, approximately 5-6 times greater than all other regions. This difference can be explained by the difference in x-component of velocity in Regions I and II, as compared to III and IV. It is apparent that regardless of location within FOV #2, the first 10 modes capture the vast majority of the energy content within the x-component of the flow field. Note that these results are averaged in the z-direction and do not help reveal any spanwise variation in spectral content. An example spatial variation of the eigenmodes in the spanwise z-direction is presented for Region I; analysis of the other regions will be pursued as future work.

To understand the spectral content of each eigenmode with respect to local porous structure length scales, the time-series of the POD temporal mode coefficients, a_n, of Region I were analyzed. The method presented here closely follows that of Zhu et al. [32]. The temporal mode coefficients, a_{mn} defined in Eq. (6) are denoted here simply as a_n (the m index that denotes time is removed for convenience). These a_n-vectors were calculated using $u'(x, y, t)$ flow fields, for every spanwise plane (i.e., 2-D POD conducted for every plane in the spanwise direction). The a_n-vectors were normalized via $\sqrt{2\lambda_n}$ and passed through a Fast Fourier Transform. From these data, the frequency of the eigenmodes were estimated as a function of Strouhal number, $St_D = fD/U_0$ and spanwise distance, z/D. An analysis of the first two modes, $n = 1$ and 2, in Region I is presented in Fig. 13.

The time-series signal at $n = 1$ reveals long time scale cycles, suggesting that this is not a flow induced behavior but possibly a product of the water tunnel itself (sloshing of the water at frequencies much less than 1 Hz) or possibly an entry-exit flow behavior linked to entrainment of fluid within the porous layer [14]. At $n = 2$, however, a strong series of

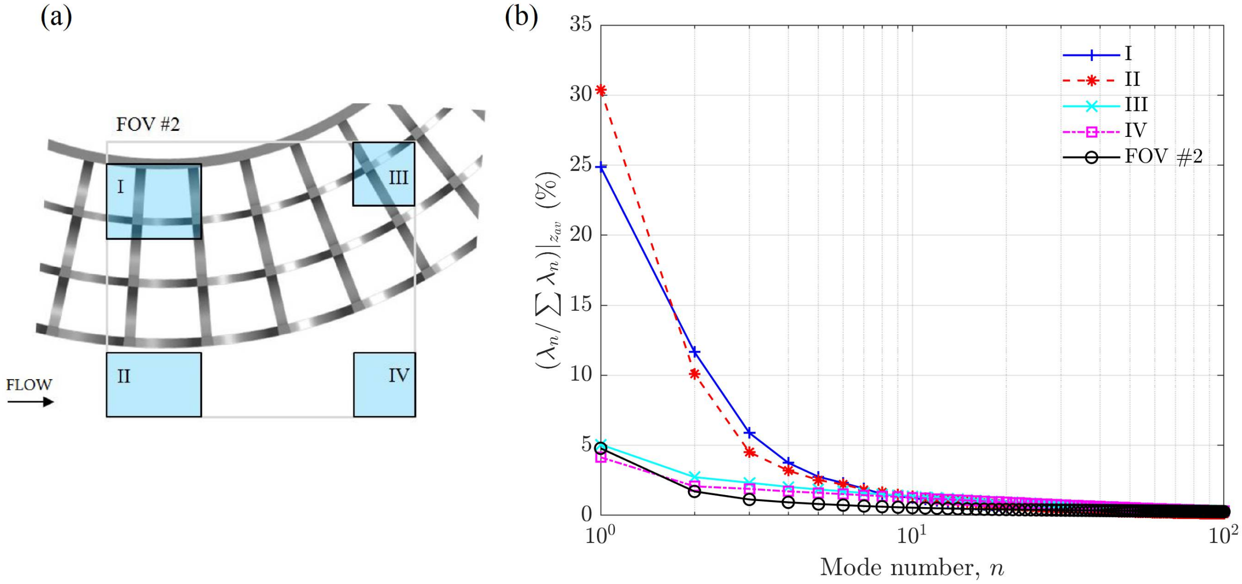

Fig. 12 (a) Location of four sub-regions in FOV #2 for POD analysis: I, II, III & IV and FOV #2, (b) POD eigenvalues, $(\lambda_n/\sum\lambda_n)|_{z_{\text{av}}}$ (%), calculated on $u'(x,y,t)$ in the regions I, II, III, IV and FOV #2 , where the subscript z_{av} denotes averaging over the spanwise z-direction.

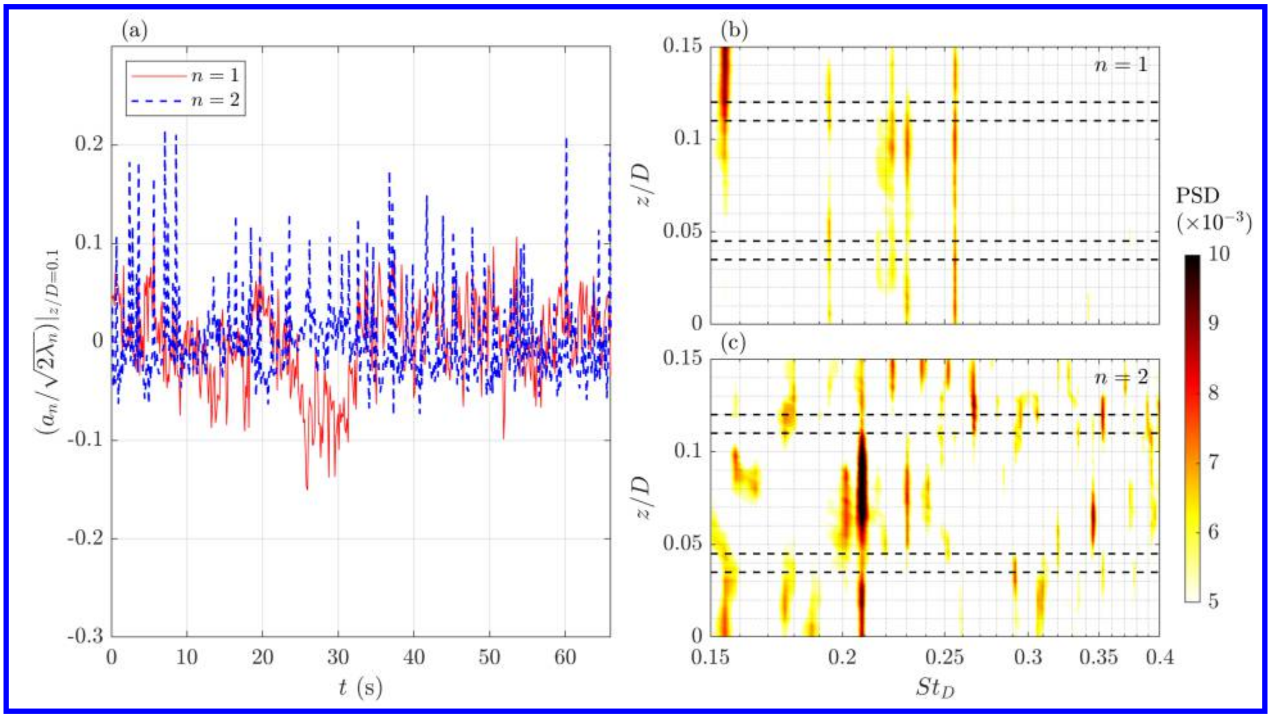

Fig. 13 (a) Time-series of the POD temporal mode coefficients, a_n, normalized using its corresponding eigenmode, λ_n, obtained at $z/D = 0.1$ within FOV #2. PSD of the POD mode coefficients are calculated at each z/D station and plotted against St_D (b) $n = 1$ and (c) $n = 2$. Closely spaced black horizontal dashed lines are drawn in (b) and (c) to identify the solid sections between the pores of the SPCC in FOV #2.

spikes in the time series are observed, and the Power Spectral Density (PSD) in Fig. 13(c) shows a strong spectral peak at $St_D = 0.21$, which is clearly linked to the vortex shedding of a cylinder in uniform flow [26]. Note the variation in strength of the spectral peak with respect to the z/D axis; $z/D \approx 0.04$ and 0.11 correspond to structural members and between them is the open pore region. In the open pore region, strong vortex shedding spectra are observed and at the structural members, as anticipated, this fades rapidly. This interesting result reveals vortex shedding within a single pore in Region I, and the rapid reduction of spectral content at the pore structural member. Other spectral content at different Strouhal numbers are scattered about various z/D-values. These may be explained by different shedding scales due to the complex flow field interaction of each pore (oriented at different angles to the x-axis) and flow field amplitude variation in the z-direction (spanwise direction).

IV. Conclusions

Tomographic PIV was conducted on a transparent SPCC in a water tunnel. This paper presented some key 3-D flow field results as part of an ongoing study into the internal and near-wall flow fields of an SPCC. From the presented data and analysis, it can be seen that deeper insight into the internal flow field of an SPCC has been obtained. By setting the porous structure as the starting point for streamlines, and using radial pathways to investigate time-averaged velocity quantities, the approach of the flow from the freestream and how it interacts with the porous layer is better understood. The interaction between the porous layer on the windward surface has now been more clearly visualized using streamlines. Three-dimensional flow fields help reveal regions of vorticity and shear as the flow passes around and into the porous layer, and evidence of flow entrainment within the windward porous layers. The development of the boundary layer profile at the mic-circumferential region coincides with regions of peak vorticity within the porous layer and regions of strong cross-correlation from upstream reference points. Using POD, velocity fluctuations at the fundamental vortex shedding frequency are observed within the porous layer, eluding to the conclusion that vortex shedding processes occur both inside and outside the porous layer.

Future work will include a similar investigation of a leeward FOV using the same post-processing techniques here (data has been already collected and partly processed). Some preliminary results have also been obtained using a square-shaped porous coated cylinder using the same tomographic PIV FOVs. A comparison between the passive flow control of the square-shaped and elliptical-shaped porous coated cylinders will be conducted, revealing which structured porous media is more effective at modifying the near-wake flow field.

Acknowledgments

This research was supported by the National Natural Science Foundation of China (Grant No. 92052105). The authors are grateful for the support from the Center for Computational Science and Engineering at the Southern University of Science and Technology.

References

[1] Zdravkovich, M. M., “Review and classification of various aerodynamic and hydrodynamic means for suppressing vortex shedding,” *Journal of Wind Engineering and Industrial Aerodynamics*, Vol. 7, No. 2, 1981, pp. 145–189.

[2] Sueki, T., Ikeda, M., and Takaishi, T., “Aerodynamic noise reduction using porous materials and their application to high-speed pantographs,” *Quarterly Report of RTRI*, Vol. 50, No. 1, 2009, pp. 26–31.

[3] Sueki, T., Takaishi, T., Ikeda, M., and Arai, N., “Application of porous material to reduce aerodynamic sound from bluff bodies,” *Fluid Dynamics Research*, Vol. 42, No. 1, 2010, p. 015004.

[4] Boorsma, K., Zhang, X., Molin, N., and Chow, L. C., “Bluff Body Noise Control Using Perforated Fairings,” *AIAA Journal*, Vol. 47, No. 1, 2009, pp. 33–43.

[5] Geyer, T. F., “Experimental evaluation of cylinder vortex shedding noise reduction using porous material,” *Experiments in Fluids*, Vol. 61, No. 7, 2020, pp. 1–21.

[6] Liu, H., Wei, J., and Qu, Z., “Prediction of aerodynamic noise reduction by using open-cell metal foam,” *Journal of Sound and Vibration*, Vol. 331, No. 7, 2012, pp. 1483–1497.

[7] Geyer, T. F., and Sarradj, E., “Circular cylinders with soft porous cover for flow noise reduction,” *Experiments in Fluids*, Vol. 57, No. 3, 2016, p. 30.

[8] Arcondoulis, E. J. G., Liu, Y., Li, Z., Yang, Y., and Wang, Y., "Structured porous material design for passive flow and noise control of cylinders in uniform flow," *Materials*, Vol. 12, No. 18, 2019, p. 2905.

[9] Wen, K., Arcondoulis, E. J., Li, Z., and Liu, Y., "Structure resolved simulations of flow around porous coated cylinders based on a simplified pore-scale model," *Aerospace Science and Technology*, Vol. 119, 2021, p. 107181.

[10] Li, Z., Tang, T., Liu, Y., Arcondoulis, E. J. G., and Yang, Y., "Implementation of compressible porous-fluid coupling method in an aerodynamics and aeroacoustics code–Part II: Turbulent flow," *Applied Mathematics and Computation*, Vol. 373, 2020, p. 124988.

[11] Zhang, P., Liu, Y., Li, Z., Liu, H., and Yang, Y., "Numerical study on reducing aerodynamic drag and noise of circular cylinders with non-uniform porous coatings," *Aerospace Science and Technology*, Vol. 107, 2020, p. 106308.

[12] Li, Z., Tang, T., Liu, Y., Arcondoulis, E. J. G., and Yang, Y., "Numerical study of aerodynamic and aeroacoustic characteristics of flow over porous coated cylinders: Effects of porous properties," *Aerospace Science and Technology*, Vol. 105, 2020, p. 106042.

[13] Yuan, Y., Xu, K., and Zhao, K., "Numerical analysis of transport in porous media to reduce aerodynamic noise past a circular cylinder by application of porous foam," *Journal of Thermal Analysis and Calorimetry*, Vol. 141, No. 5, 2020, pp. 1635–1646.

[14] Naito, H., and Fukagata, K., "Numerical simulation of flow around a circular cylinder having porous surface," *Physics of Fluids*, Vol. 24, No. 11, 2012.

[15] Xu, C., Mao, Y., and Hu, Z., "Numerical study of pore-scale flow and noise of an open cell metal foam," *Aerospace Science and Technology*, Vol. 82, 2018, pp. 185–198.

[16] Arcondoulis, E. J. G., Geyer, T. F., and Liu, Y., "An investigation of wake flows produced by asymmetrically structured porous coated cylinders," *Physics of Fluids*, Vol. 33, No. 3, 2021, p. 037124.

[17] Arcondoulis, E. J., Geyer, T. F., and Liu, Y., "An acoustic investigation of non-uniformly structured porous coated cylinders in uniform flow," *The Journal of the Acoustical Society of America*, Vol. 150, No. 2, 2021, pp. 1231–1242.

[18] Arcondoulis, E., Liu, Y., Yang, Y., Ragni, D., Rubio Carpio, A., and Avallone, F., "Internal and Near-Wall Flow Fields of a Structured Porous Coated Cylinder and Their Role in Passive Flow and Noise Control," *AIAA Aviation 2021 Forum*, 2021, p. 2226.

[19] Yu, H., Xu, Z., Chen, W.-L., Li, H., and Gao, D., "Attenuation of vortex street by suction through the structured porous surface," *Physics of Fluids*, Vol. 33, No. 12, 2021, p. 125101.

[20] JCR, H., Wray, A., and Moin, P., "Eddies, stream, and convergence zones in turbulent flows," *Studying Turbulence Using Numerical Simulation Databases-I1*, Vol. 193, 1988.

[21] Liu, H., and Azarpeyvand, M., "Passive Control of Tandem Cylinders Flow and Noise Using Porous Coating," *Proceedings of the 22nd AIAA/CEAS Aeroacoustics Conference*, 2016.

[22] Aguiar, J., Yao, H., and Liu, Y., "Passive Flow/Noise Control of a Cylinder Using Metal Foam," *Proceedings of the 23rd International Congress on Sound and Vibration*, 2016, pp. 1–8.

[23] Xia, C., Wei, Z., Yuan, H., Li, Q., and Yang, Z., "POD analysis of the wake behind a circular cylinder coated with porous media," *Journal of Visualization*, Vol. 21, No. 6, 2018, pp. 965–985.

[24] Arcondoulis, E., Ragni, D., Rubio Carpio, A., Avallone, F., Liu, Y., Yang, Y., and Li, Z., "The internal and external flow fields of a structured porous coated cylinder and implications on flow-induced noise," *Proceedings of the 25th AIAA/CEAS Aeroacoustics Conference*, 2019.

[25] Ruck, B., Klausmann, K., and Wacker, T., "The flow around circular cylinders partially coated with porous media," *AIP Conference Proceedings*, Vol. 1453, No. 1, 2011, pp. 49–54.

[26] Norberg, C., "Fluctuating lift on a circular cylinder: review and new measurements," *Journal of Fluids and Structures*, Vol. 17, No. 1, 2003, pp. 57–96.

[27] Jenkins, L., Neuhart, D., McGinley, C., Khorrami, M., and Choudhari, M., "Measurements of unsteady wake interference between tandem cylinders," *Proceedings of the 36th AIAA Fluid Dynamics Conference and Exhibit*, 2006, p. 3202.

[28] Neuhart, D., Jenkins, L., Choudhari, M., and Khorrami, M., "Measurements of the flowfield interaction between tandem cylinders," *Proceedings of the 15th AIAA/CEAS Aeroacoustics Conference*, 2009.

[29] Hutcheson, F. V., Brooks, T. F., Lockard, D. P., Choudhari, M. M., and Stead, D. J., "Acoustics and Surface Pressure Measurements from Tandem Cylinder Configurations," *Proceedings of the 20th AIAA/CEAS Aeroacoustics Conference*, 2014.

[30] Chen, W.-L., Gao, D.-L., Yuan, W.-Y., Li, H., and Hu, H., "Passive jet control of flow around a circular cylinder," *Experiments in Fluids*, Vol. 56, No. 11, 2015, p. 201.

[31] Yang, Y., Pröbsting, S., Liu, Y., Zhang, H., Li, C., and Li, Y., "Effect of dual vortex shedding on airfoil tonal noise generation," *Physics of Fluids*, Vol. 33, No. 7, 2021, p. 075102.

[32] Zhu, H.-Y., Wang, C.-Y., Wang, H.-P., and Wang, J.-J., "Tomographic PIV investigation on 3D wake structures for flow over a wall-mounted short cylinder," *Journal of Fluid Mechanics*, Vol. 831, 2017, pp. 743–778.